

AUTOMATICALLY DETECTING AND TRACKING CMES I: THE SEPARATION OF DYNAMIC AND QUIESCENT COMPONENTS IN CORONAGRAPH IMAGES

HUW MORGAN^{1,2}, JASON P. BYRNE² & SHADIA RIFAI HABBAL²

¹Sefydliad Mathemateg a Ffiseg, Prifysgol Aberystwyth, Ceredigion, Cymru, SY23 3BZ and

²Institute for Astronomy, University of Hawaii, 2680 Woodlawn Drive, Honolulu, HI 96822, USA

Draft version January 17, 2012

ABSTRACT

Automated techniques for detecting and tracking CMEs in coronagraph data are important for statistical studies and for space weather monitoring. They require distinguishing the CME structure from the background quiescent coronal structure (streamers, coronal holes). Many studies resort to some form of time-differencing to achieve this, despite the errors inherent in such an approach - notably spatiotemporal crosstalk. This article describes a new deconvolution technique which separates coronagraph images into quiescent and dynamic components. A set of synthetic observations made from a sophisticated corona and CME model demonstrates the validity and effectiveness of the technique in isolating the CME signal. Applied to observations by the LASCO C2 and C3 coronagraphs, the structure of a faint CME is revealed in detail despite the presence of background streamers which are several times brighter than the CME. The technique is also demonstrated to work on SECCHI/COR2 data, and new possibilities for estimating the 3D structure of CMEs using the multiple viewing angles are discussed. Quiescent coronal structures and CMEs are intrinsically linked, and must interact (for example, CMEs often cause rapid changes in streamer brightness and position). Although such interaction is an unavoidable source of error in any separation process, we show in a companion paper that the deconvolution approach is a robust and accurate method as a prerequisite to the higher-level detection and classification of CME structure and kinematics.

Subject headings: Sun: corona—sun: CMEs—sun: solar wind

1. INTRODUCTION

A coronal mass ejection (CME) was first observed scientifically during the total solar eclipse of 1860, but it was not recognized as an important dynamic phenomenon (see Eddy (1974)). The first modern discovery of CMEs, and the frequency of their occurrence, was made by the white light coronagraphic observations of the Skylab mission in the early 1970s (see Gosling et al. (1974), and references within). CMEs are energetic clouds of magnetic plasma ejected by the Sun into interplanetary space. They have a large range of sizes, masses and velocities. They are associated with the eruption of filaments, and/or solar flares and/or no apparent trigger event. The Large Angle Spectrometric Coronagraph (LASCO) onboard the Solar and Heliospheric Observatory (SOHO, Brueckner et al. (1995)) enabled a great advance in our understanding of the dynamic corona, and paved the way for the Sun Earth Connection Coronal and Heliospheric Investigation (SECCHI, Howard et al. (2002)) coronagraphs on the Solar TErrestrial RElations Observatory (STEREO) spacecraft. In the last decade, CME events (and their spatial size, type and distribution, velocity and acceleration) have been detected and catalogued using manual (Yashiro et al. 2004) and automated (Robbrecht & Berghmans 2004; Olmedo et al. 2008) methods, enabling detailed statistical analysis and revealing correlation with other solar events (for example, Gopalswamy et al. (2001) or Bewsher et al. (2008)). A more detailed introduction to the field is given in a companion paper: Byrne et al. (2011), referred to as Paper II throughout this article.

Many aspects of CME initiation and subsequent evolution demand better understanding, and this can only be gained by more information on CME structure, density, and other physical attributes. When viewed in white light coronagraph images, their emission is integrated over an extended line-of-sight (LOS), a LOS which includes other non-CME structures as well as the CME itself. Despite the increasing sophistication of solar tomography techniques (see Morgan et al. (2009); Morgan & Habbal (2010b), and references within), in general, detailed information is lacking on these non-CME structure (i.e. the quiescent coronal structure of streamers and coronal holes). Therefore CMEs are observed not in isolation but in the presence of bright streamers and coronal holes which are objects with their own fine structural detail. Even the basic steps of detailed CME analysis (for example, automated detection/cataloging, or an estimate of 3D density structure) is made difficult if not impossible by the presence of quiescent coronal structure within the same region of the coronagraph images. Frazin et al. (2009) shows that, given reasonable assumptions on the nature of CME structure, it is possible to reconstruct the 3D density structure of CMEs from only three field of views. One of the main hindrance to the reconstruction is the presence of quiescent coronal structure in the coronagraph data.

This work is the first of two papers which aim to improve the automated detection and cataloging of CMEs. Paper II is concerned with a sophisticated set of algorithms, based on wavelet edge detection techniques outlined by Byrne et al. (2009), which automatically detect and track CMEs in coronagraph data. To greatly improve the detection process, the coronagraph data are

first processed to reduce the signal of quiescent coronal structure. The process described in this article is based on an iterative deconvolution in time and space which aims to isolate the CME and the quiescent corona components in a white light image, resulting in separate images of the CME, and the background corona without a CME. Another process based on least-squares fitting of quiescent coronal structure to polynomials was introduced by Morgan & Habbal (2010a). That process, although successful, lacks elegance and has not been rigorously tested on a model dataset. It also does not take full advantage of the time dimension of the data. To test the validity of the new technique, section 2 constructs a model CME and corona from which synthetic coronagraph observations can be made. Section 3 describes a deconvolution-based process to separate the quiescent structure from the dynamic events. Section 4 shows the results of applying the process to both the model observations and real observations made by the LASCO C2 and C3 coronagraphs. The process is discussed in section 5 and conclusions are given in section 6.

2. A MODEL CORONA AND CMES

The description of the method is aided by the use of a time series of synthetic coronagraph observations. These are created from a 3D density model of the corona through which model CMEs of various shapes and orientation are propagated. Later in the article, the synthetic data can be used to test the effectiveness of the separation method. Here we describe the model corona, and the synthetic observations made from the model densities. The aim is to create coronagraph-type images, with field of view (FOV) properties similar to the observations made by the LASCO C2 and C3 coronagraphs.

To create the model corona observations, a 3D xyz grid of size 1024^3 is constructed. Model coronal densities are distributed throughout the cube so that the centre voxel of the cube is at the position of Sun center (a voxel is the 3D equivalent of a pixel, forming one element of the grid). As the corona rotates and the B_0 angle (relative angle of the Sun's rotation axis and the Sun-Earth line) changes with time, the model densities are rotated within the cube, so that the x axis always lies along the Sun-observer direction. The densities are integrated using appropriate geometrical scattering weights along the x -axis (or line of sight (LOS)), resulting in a 1024×1024 image along the y and z axes. The whole process is repeated twice for two FOVs. For the LASCO C2-type synthetic observations, the extent of the y and z axes is $\pm 6R_\odot$, whilst $\pm 30R_\odot$ is used for the C3-type observations. The extent of the x axis (along the LOS) depends on $\sqrt{y^2 + z^2}$, or the height of the pixel in the final image, so that pixels at large heights have an appropriately long line of sight.

The density distributed through the model cube is determined empirically. Tomographic reconstructions have been made of the solar corona over a whole solar cycle using LASCO C2 observations (Morgan et al. 2009; Morgan & Habbal 2010b). A map of the coronal density structure reconstructed for a two-week set of observations centered on 2005/01/18 (CR 2025.6) is shown in figure 1. The choice of date is arbitrary, but a clean reconstruction with streamers distributed up to high mid-latitudes was preferred. This longitude-latitude map is

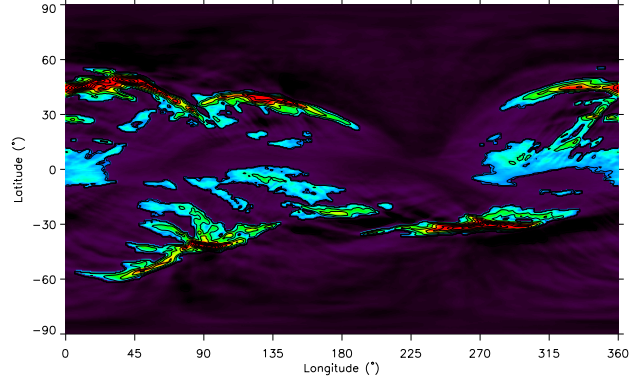


FIG. 1.— Tomographic reconstruction of the coronal density structure at a height of $4R_\odot$ created from LASCO C2 data collected over a half-solar-rotation period centered on 2005/01/18 (CR 2025.6). Lowest density regions are black to purple, whilst higher density streamers range from light blue through green, yellow, to red. The reconstruction map has 720 longitude bins, and 360 latitude bins. As explained in the text, density units are normalized (not absolute electron density).

a shell of the corona at $4R_\odot$, and the density is in normalized units (not absolute electron density, see Morgan et al. (2009)). The depicted structure shows accurately the distribution of streamers during the observational period, and the structure is used as a basis to create a set of synthetic coronal observations. To achieve this, the coronal structure is assumed to be radial, so the structure shown at $4R_\odot$ is extrapolated appropriately through all heights above $1R_\odot$ in the model corona. At any given height, the highest density point has value 1 and lowest has value 0 since the density is normalized.

The normalized density distribution must be converted to an appropriate absolute electron density. To achieve this, regions of the corona with low density (values close to zero), are given the density height profile found by Doyle et al. (1999) for polar coronal holes. Regions with high density (values close to one) are given the density height profile found by Guhathakurta et al. (1996). Regions with values between 0 and 1 are given a weighted sum of the two height-density profiles, in a manner similar to Gibson et al. (2003). Specifically, the density at a given longitude θ , latitude ϕ and heliocentric height r , $\rho(\theta, \phi, r)$ is given by

$$\rho(\theta, \phi, r) = \rho_n(\theta, \phi)n_{st}(r) + [1 - \rho_n(\theta, \phi)]n_{ch}(r), \quad (1)$$

where $\rho_n(\theta, \phi)$ is the normalized longitude-latitude density map shown in figure 1, $n_{st}(r)$ is the height profile of density described by Guhathakurta et al. (1996):

$$n_{st}(r) = [3.6r^{-15.3} + 0.99r^{-7.34} + 0.365r^{-4.31} + (5.8 \times 10^{-3})r^{-2}] \times 10^8, \quad (2)$$

and $n_{ch}(r)$ is the height profile of density described by Doyle et al. (1999):

$$n_{ch}(r) = (1 \times 10^8)r^{-8} + (2.5 \times 10^3)r^{-4} + (2.9 \times 10^5)r^{-2}. \quad (3)$$

Note that a r^{-2} term has been added to the Guhathakurta et al. (1996) density profile, in order to achieve a well-behaved density profile at large heights.

For a given date, the Carrington longitude and B_0 angle of the Sun-observer direction is calculated, and the 3D density profile rotated appropriately within the xyz grid.

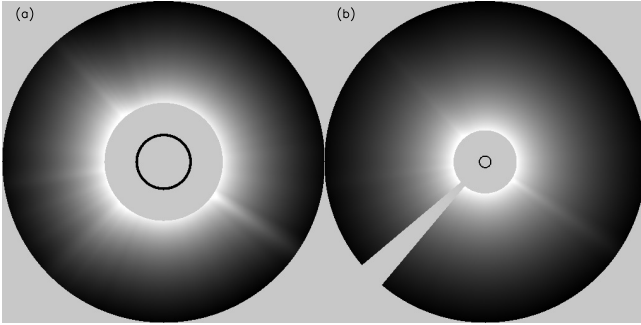


FIG. 2.— Synthetic coronal brightness images created for (a) a C2-type FOV and (b) a C3-type FOV for observation time 2005/01/18 04:56 (that is, the model corona is rotated to an appropriate Carrington longitude and B_0 angle for this time). The inner black circle shows the position of the Sun. \log_{10} of brightness is shown, with a little contrast enhancement.

The geometric scattering coefficients for total brightness Thomson scattering (van de Hulst 1950; Quémérais & Lamy 2002) are calculated, and are multiplied by the density and the LOS increment throughout the grid. The grid is integrated along the x axis, forming a total brightness image. Examples of synthetic images are shown in figure 2. A time series of such images is formed by rotating the density model, with a cadence of one observation per half-hour, similar to the LASCO coronagraphs. These form the quiescent coronal images to which a propagating CME will be added.

To test the model, six CMEs are launched. Three are simple small blobs of varying density. These are spheres with a Gaussian drop in density with distance from the sphere center. The other three are hollow flux tubes which loop from two footpoints on the Sun into the corona. By parameterizing the normalized height z_{cme} along the central axis of the flux tube by a path length s which ascends from the Sun's surface ($z_{cme} = 0, s = 0.0$) to the maximum CME height ($z_{cme} = 1, s = 0.5$) then descends along the same path to the Sun's surface ($z_{cme} = 0, s = 1.0$), the shape of the loop may be easily adapted. For a given observation time, the CME structure is scaled according to the maximum height of the CME ($z_{cme} = 1$) which is a function of CME launch time, velocity and acceleration. Given the set of xyz coordinates which describe the central path of the hollow flux tube through the corona, a regularly-spaced set of $y - z$ points are defined which encompass all points within the desired final image which will contain any appreciable CME signal. Typically, this is a set of several hundred pixels for which the CME brightness will be calculated. For each pixel, a line of sight is defined which, again, is limited to a range which will contain some CME structure. Each line of sight has a hundred or so points, therefore a computing space of around a million voxels is used to create the CME images. Limiting the number of voxels in this way greatly increases the computational efficiency in comparison to, for example, simply calculating the images for a whole-corona FOV. The minimum distance d from each voxel to the central CME axis is calculated. Given d , it is simple to define a normalized CME density structure ρ_{cme} as

$$\rho_{cme} = \exp(-[(d - w(r))/\sigma(r)]^2), \quad (4)$$

CME	Type	Launch	V	Lon	Co-lat	Inc	ρ_{rel}
A	Loop	00:09	600	-90	90	90	1
B	Loop	00:09	600	30	80	70	1
C	Loop	07:12	600	-50	60	50	1
D	Blob	08:43	500	90	135	-	1/2
E	Blob	11:44	500	90	135	-	1/4
F	Blob	16:16	500	90	135	-	1/10

TABLE 1

DETAILS OF THE SIX CMEs. NEGATIVE (POSITIVE) LONGITUDES ARE TOWARDS THE EAST (WEST) RELATIVE TO THE SUN-OBSERVER LINE. AN INCLINATION OF 0° (90°) MEANS THE LOOP IS EDGE-ON (FACE-ON) TO THE OBSERVER. THE 'LOOP' TYPE IS THE HOLLOW FLUX TUBE DESCRIBED IN THE TEXT. 'BLOB' IS THE SPHERICALLY SYMMETRIC GAUSSIAN. ρ_{rel} IS THE RELATIVE DENSITY OF THE CME AT A GIVEN HEIGHT COMPARED WITH THE DENSITY SPECIFIED IN EQUATION 2. THE LAUNCH COLUMN GIVES THE TIME THE CME IS LAUNCHED FROM THE SUN ON DATE 2005/01/18. ALL ANGLES ARE IN DEGREES, AND VELOCITY IN km s^{-1} .

where $w(r)$ sets the radius of the hollow flux tube (set to expand with height r), and $\sigma(r)$ sets the width of the density profile from the tube edges, similarly set to expand with height. This hollow flux tube, looping out into the corona, is similar to the flux rope model used by Thernisien et al. (2006).

An adjustment is made to account for the disappearance of the CME with time, by multiplying by the function

$$\rho'_{cme} = \rho_{cme} \exp(-[(r - r_{max})/\sigma'(r)]^2), \quad (5)$$

where r_{max} is the height of the leading edge of the CME. This adjustment ensures that the legs of the CME fade and disappear as the CME propagates to large heights. The normalized CME density structure is changed to absolute electron density simply by multiplying by the density height profile given by equation 2 and a constant factor. Given geometrical scattering coefficients, LOS integrations are made along the x axis, giving a set of $y - z$ points describing the CME image brightness. Similar to the coronal model, the xyz coordinate system is adapted according to the propagation of the CME and the slow rotation of the corona, and a time series of CME observations is made. The CME images, since they are composed of non-gridded $y - z$ points, are interpolated (using a cubic spline) to the regular $y - z$ grid of the model coronal images. Example images of the CMEs are shown in figure 3. Details of all six CMEs are listed in table 1. Each CME is labeled for convenience A-F. They are all launched on 2005/01/18 with a constant velocity - the loops at 600 km s^{-1} and the blobs at 500 km s^{-1} . The three blobs are identical except for varying density (listed as ρ_{rel} in the table), to test the sensitivity of the procedures.

Finally, the coronal and CME images are combined by summing. Examples of the combined coronal and CME images will be shown in the following section. The combined images will be used as a test for the CME-quiescent coronal separation process, and, further, as a test for the higher-level automated detection and tracking procedures in Paper II. For this purpose, three days of model coronal images are created, at a cadence of 30 minutes (a total of 144 images per FOV). The dates of these observations are 2005/01/17 00:00 through to 2005/01/19 23:59. The CMEs are launched on the second day, according to the launch times given in table 1. Random Gaussian noise with a standard deviation of

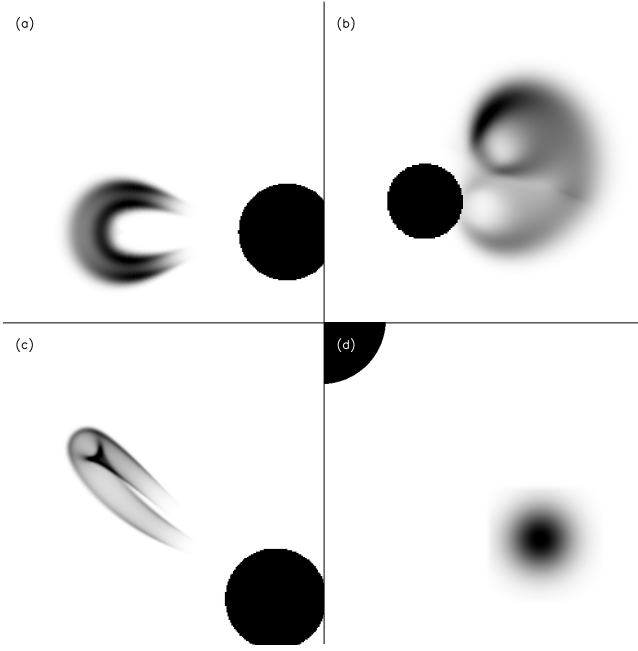


FIG. 3.— Synthetic CME brightness images created for four of the six CMEs listed in table /refcmetable. (a) Hollow flux tube looping out into the corona, with front edge at height $5R_{\odot}$. The loop is viewed face-on, and the central axis of symmetry of the loop is at longitude -90° relative to the observer (in the plane of the sky in the east), and co-latitude 90° (equator). This is CME A (see table 1). CME (b) B, (c) C, and (d) D. The black circle/part of a circle in each image shows the position of the Sun. Log₁₀ of brightness is shown, with a little contrast enhancement. Shades are reversed, so that black regions are the brightest.

$3 \times 10^{-14} B_{\odot}$, and smoothed by a 3×3 sliding window, is added to each image. Noise of this nature seems to replicate the appearance of noise in LASCO C3 images well, as can be seen in following images. The same noise level is added to the C2-type model images but the noise level is very small compared to the signal at low heights, as is the case with the real data.

3. THE SEPARATION PROCESS

3.1. The Normalising Radial Graded Filter (NRGF)

The CME-quiescent corona separation process is based on the fact that the quiescent coronal structure is extended radially in structure above $\sim 2.5R_{\odot}$, and changes only slowly in time. CMEs, on the other hand, are not extended radial structures, and change rapidly in time. Therefore the first step in the separation process is to reveal the radial structure of the corona. This is achieved using the Normalizing Radial Graded Filter (NRGF) described by Morgan et al. (2006). Figure 4a shows an unprocessed model coronal image (no CMEs). The image is dominated by the steep radial drop in brightness. The mean brightness as a function of height is plotted as the solid line in figure 4b, and the standard deviation is shown as a dashed line. Any structural information contained in the image is lost since the contrast within the image is dominated by these functions, which range over several orders of magnitude. Whilst the important physical information is contained in the original calibrated brightness units (absolute electron density, for example), the image is not useful for viewing the underlying coronal structure. The coronal structure can be effectively (and

correctly) revealed by the simple equation

$$I'(r, \phi) = \frac{I(r, \phi) - I(r)_{<\phi>}}{\sigma(r)_{<\phi>}} \quad (6)$$

where $I'(r, \phi)$ is the processed and $I(r, \phi)$ is the original intensity at height r and position angle ϕ , and $I(r)_{<\phi>}$ and $\sigma(r)_{<\phi>}$ are the mean and standard deviation of intensities calculated over all position angles at height r . In this paper, the term ‘NRGF brightness’ is often used, and it means $I'(r, \phi)$, or the image brightness values after transformation using equation 6.

The application of equation 6 to figure 4a is shown in 4c. The true radial nature of the model corona has been effectively revealed using a simple transformation. An important property of this transformation is it can be reversed so that the original brightness units can be regained. Since the average and standard deviation of brightness, as functions of heights, have been calculated for large groups of pixels, the process does not amplify noise within an image. The NRGF has been used as a tool for revealing coronal structure in many studies (Morgan & Habbal (2007a,b, 2010b); He et al. (2009); Wang et al. (2010); Kienreich et al. (2009); Lugaz et al. (2009); Frazin et al. (2009); Habbal et al. (2007, 2011), for example), and has been further developed in the sophisticated Fourier-NRGF (Druckmüllerová et al. 2011).

Despite the simplicity of equation 6, some care needs to be taken with its application to real data. The following steps describe how the NRGF is applied to large sets of LASCO data:

- Bad regions within images must be identified and avoided in subsequent processing.
- Point filters are applied to avoid spikes.
- The mean and standard deviation of brightness are calculated for approximately a hundred height bins throughout the field of view. This ensures a large number of pixels to each height bin.
- The mean and standard deviation profiles are smoothed using a wide sliding window median to avoid bad values caused by errors in the image.
- Before processing the image with equation 6, mean and standard deviation profiles collected over several dozen observations (a day or even several days) are recorded. From these a median mean and standard deviation is created. These are the profiles which are then used to process the images. Calculating a long-term mean and standard deviation in this way reduces the influence of large CMEs and other sources of errors on the height profiles.

Many of these steps are unnecessary for model data, but are nevertheless applied to the set of synthetic images. Figure 5 shows the result of applying the NRGF process to combined model corona, CME and noise C2 and C3-type images.

3.2. Quiescent-dynamic separation by deconvolution

An iterative scheme is applied to the synthetic data to separate the quiescent and CME components. For computational convenience, the images are converted to

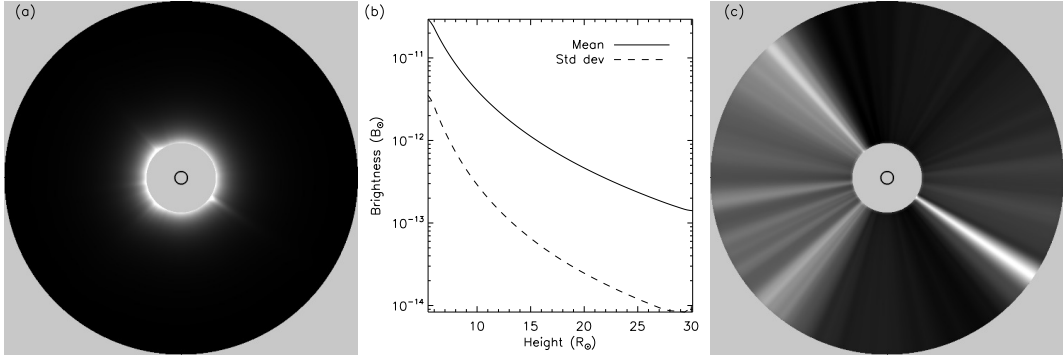


FIG. 4.— (a) Unprocessed synthetic coronal image showing a C3-type FOV. The small inner circle shows the position of the Sun. (b) Mean (solid line) and standard deviation (dashed line) as a function of height calculated from the image shown in (a). (c) Image (a) processed using equation 6. Note how the true radial structure of the model corona is effectively revealed by the simple process.

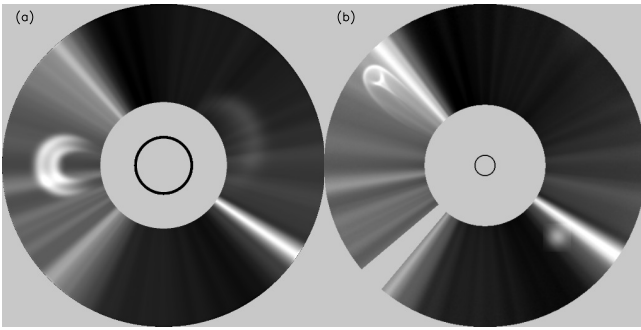


FIG. 5.— Synthetic images containing the model corona, CMEs and noise for (a) 2005/01/18 01:10, C2 FOV ($2.25\text{-}5.75R_{\odot}$) and (b) 2005/01/18 12:14, C3 FOV ($6.0\text{-}16.0R_{\odot}$) FOV. These images have been processed with the NRGF. The CMEs shown are the ones shown in isolation in figure 3, namely CMEs A and B in (a), and C and D in (b).

polar coordinates. An example is shown in figure 6a for the C2-type FOV. Figure 6b shows four radial cuts through the polar image. The two cuts without CMEs are close to constant across all heights. This shows that the model corona is radial and that the NRGF is an effective process to reveal the large-scale structure. The CME is clearly seen in the other two profiles as a large enhancement in brightness. Figure 6c shows brightness time profiles throughout 2005/01/18 at a height of $5.5R_{\odot}$ at each of the four position angles. The coronal hole brightness remains constant, whilst the streamer (without CME) brightness decreases slowly throughout the day. The CME profiles show a sharp enhancement during the passage of the CME. The CME front edge is enhanced for one observation only at this height (\sim half hour). The CME leg remains enhanced for three observations (\sim hour and a half). Time-differencing is a commonly used method to reveal CMEs in coronagraph images, and these time profiles illustrate both the strength and weakness of this method. The CME is a sharp enhancement in time, so time-differencing will reveal the CME clearly. However, a simple frame-to-frame time-differencing will introduce large errors, and create unwanted artifacts which can easily be misinterpreted as CME structure. The fact that the CME front edge occupies one observation whilst the leg remains for three is one simple argument that illustrates this error. In addition, quiescent coronal structure changes brightness considerably (even for a model CME where the actual

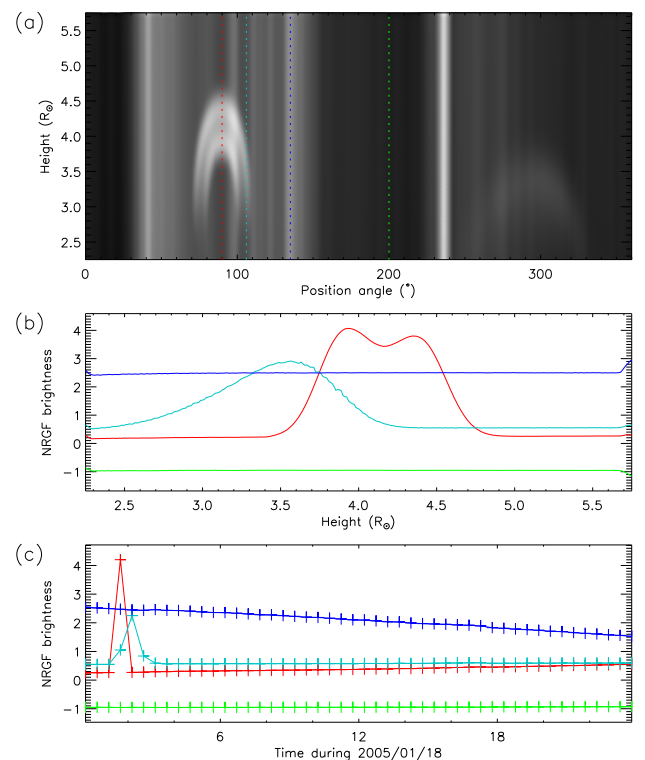


FIG. 6.— (a) NRGF-processed image of figure 5a transformed into polar coordinates. The x-axis shows position angles anti-clockwise from North, and the y-axis shows heliocentric height throughout the useful FOV. Two CMEs (A and B) can be seen in this image. A is bright at position angle 90° , and B is a faint halo seen centered at position angle 290° . Four radial slices are chosen at position angles 90° (red, cutting through CME front), 106° (cyan, cutting through CME leg), 135° (blue, streamer without CME) and 200° (green, coronal hole without CME). (b) Radial profiles of NRGF brightness along the four cuts shown in (a). (c) Time profiles of NRGF brightness along the cuts shown in (a), at a height of $5.5R_{\odot}$.

density structure remains the same), therefore long-term time-differencing will always contain considerable unwanted signal from the quiescent corona.

The CME component is separated from the quiescent component by the following iterative scheme. The scheme is based on the assumption that the quiescent corona background will always be smoother than the CME component in both radial and time dimensions. Smoothing the original signal in these dimensions there-

fore gives a signal closer to the original corona if the CME had not occurred. Subtracting this estimate of the quiescent corona from the original signal gives an estimate of the CME signal.

1. Choose one radial and time cut $X(r, t)$ at a given position angle. X is a bidimensional array with dimensions radius r and time t . Typically, r has 500 bins and $t \sim 50$ bins (one day's worth of observation given a regular half-hour cadence). The size of X varies with real data. To avoid edge effects in the time dimension, the time dimension of X is allowed to overlap to the previous and following day.
 2. Set first estimate of background as $B^0 = X$
 3. Convolve B^0 with kernel k to give the smoothed array B_s^0 ,
- $$B_s^0 = B^0 \otimes k. \quad (7)$$
- k has a Gaussian profile in the radial dimension, with FWHM of $0.67R_\odot$.
4. Subtract B_s^0 from X and constrain the result to be zero or positive to gain the first estimate of CME signal C^0 :
- $$C^0 = (X - B_s^0) > 0 \quad (8)$$
5. Make next estimate of background as $B^1 = X - C^0$.

The process is iterated from steps 3-5. In summary, the quiescent component is calculated at iteration number n as

$$B^n = X - [(X - [B^{n-1} \otimes k]) > 0]. \quad (9)$$

This is a deconvolution of the CME signal and convergence is swift. When the convergence rate drops below a preset level, a one iteration convolution is applied along the time direction rather than the radial direction. The steps are identical to the above, but with a constant kernel of width 3 observations in the time direction (so a sliding window average of width ~ 1.5 hours in the well-behaved regular case of the model data. This of course varies for real data). Iteration then returns to the radial convolution. The process is terminated according to a preset convergence rate threshold or a maximum number of iterations, and the final CME component is given by $C = X - B^n$. Figure 7 shows how the radial profile at position angle 90° (a cut through CME A's front edge, shown in figure 6), gradually converges from the original signal to a CME and a quiescent component.

This process is repeated for each position angle bin throughout the polar image. The result is an array in polar coordinates containing the estimate of the background quiescent corona. Due to the nature of the separation process, this array is smooth in the time and radial direction, relative to the original polar array. This polar array is interpolated back to the cartesian coordinates of the original NRGF images, and is then subtracted to give the CME component in full spatial resolution.

4. RESULTS

4.1. Application to synthetic data

The obvious advantage of testing the separation process on model data is that synthetic observations can be

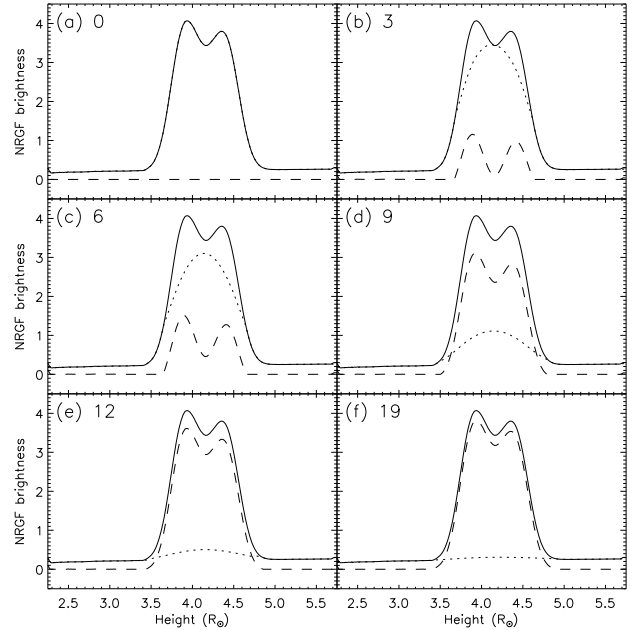


FIG. 7.— Iteration development of the CME/quiescent separation process. Each panel shows the original radial profile (solid line), CME component (dashed line) and quiescent corona (dotted line) at the stage of iteration n shown in the panel (0, 3, 6, 7, 9, 12, and 19). The example shown is a cut across the front edge of CME A at position angle 90° . Note that in panel (a) (iteration 0, or prior to deconvolution), that initial values are shown, so that the background is identical to the original profile and that the CME profile is zero at all heights.

made of the CME in the absence of the background quiescent corona, against which the separated images can be compared. For the purpose of automatically detecting and tracking CMEs, the most important aspect for accuracy is a qualitative depiction of CME structure. A good quantitative agreement is also desirable, particularly for further analysis of CME density.

Figure 8 shows a comparison of the model CME brightness compared to the CME component obtained by the separation method for the C2-type FOV for each of the three structured loop-type CMEs. The top two panels show simple contrast-enhanced images of the CMEs. There is excellent qualitative agreement between the images. The third panel shows brightness profiles, or ‘cuts’ across the images. These show that the NRGF brightness of the separated CME component is quantitatively very accurate. The bottom panel shows the relative error throughout the CME region of the image, given by $100 \times (B_{sep} - B_{mod}) / B_{mod}$, where B_{mod} is the model CME brightness (NRGF brightness), and B_{sep} is the separated CME component brightness. The average and standard deviation of the relative error is -0.6 ± 2.6 , -2.7 ± 3.1 , and $1.5 \pm 3.7\%$ for CME A, B and C respectively.

Figure 9 shows similar results for the C3-type FOV. The average and standard deviation of the relative error is in this case -4.2 ± 3.5 , -6.8 ± 3.4 , and $2.0 \pm 4.5\%$. In general, the average relative error is a small, and is a systematic error due to inaccuracies in the separation process. The spread of the relative error becomes greater for lower brightness CMEs as the signal-to-noise decreases. CME B (the large halo CME) has the most negative relative error due to the CME being a large, smooth struc-

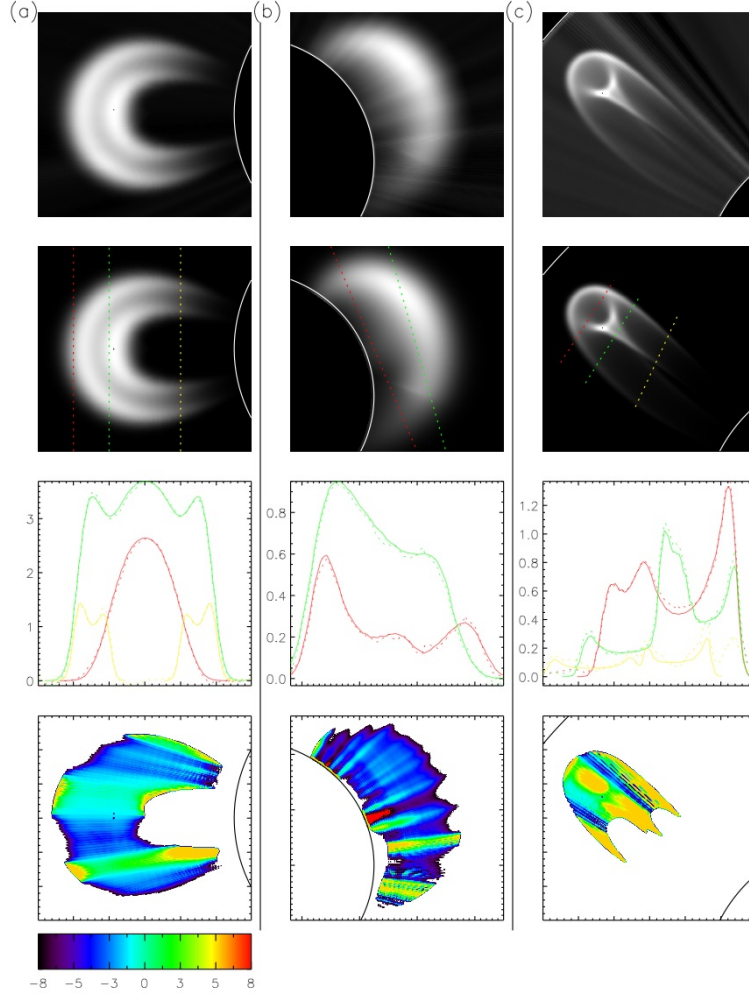


FIG. 8.— Comparison of direct model CME observations and the separated CME component for the C2-type FOV. The three columns (a), (b), and (c) are for CMEs A, B and C. The two top panels of each column compare a NRGF image of the separated CME component and the model CME. The white curved lines show the limits of the FOV. Three colored dashed lines are plotted over the model CME images. Slices of the NRGF brightness along these lines are plotted in the third column for the model CME (thick line) and separated CME component (thin line). In many places, these two lines are indistinguishable. The fourth panel shows the percent relative difference between the model and separated CME brightness, with colors indicated by the color bar.

ture, with a greater smooth radial extent than the other CMEs. Since this is a halo CME (moving towards the observer), the apparent velocity is small therefore the CME has smaller changes in time. Both the slow time changes and the smoother radial profile causes more of the CME component to be wrongly included with the quiescent component. In contrast, CME C has a positive relative error. CME C is more finely structured than the other CMEs, and is overlaid on a region of the corona containing many fine streamer substructures. The separation process includes some of this quiescent structure in the CME component leading to an overestimation of CME brightness.

Figure 10 shows a comparison of model and separated NRGF brightness for the three blob type CMEs (D, E and F). The separation process gives excellent results for these CMEs, with only a few percent relative error for the faintest CME (CME F) in the LASCO C3 FOV. The systematic error is a small overestimation of the CME brightness by the separation process for the LASCO C3 FOV. Note that CME F is very faint, with a density only

10% that of streamers at the same height.

4.2. Application to LASCO C2 and C3 data

Figures 11 and 12 show the result of applying the CME separation process to LASCO C2 and C3 observations of a faint CME during 2010/03/12. This CME is a challenging test of the method for two main reasons: it is a relatively faint CME, and it is propagating in the same region of the image as a complicated streamer structure. As can be seen from the figures, the separation method is very effective at revealing the CME structure. In the original image, it is almost impossible to interpret CME structure since the image is dominated by the bright streamers. The separated CME component shows how very faint the CME is compared to the streamers. The brightest part of the CME is the knotted inner ‘eye’, centered at $3R_{\odot}$ in the C2 image. By the C3 image, this knotted structure is not apparent. The front edge of the CME is very faint, as can be seen in figure 12f – around a fifth of the background streamer signal at the same height. That the separation process is successful

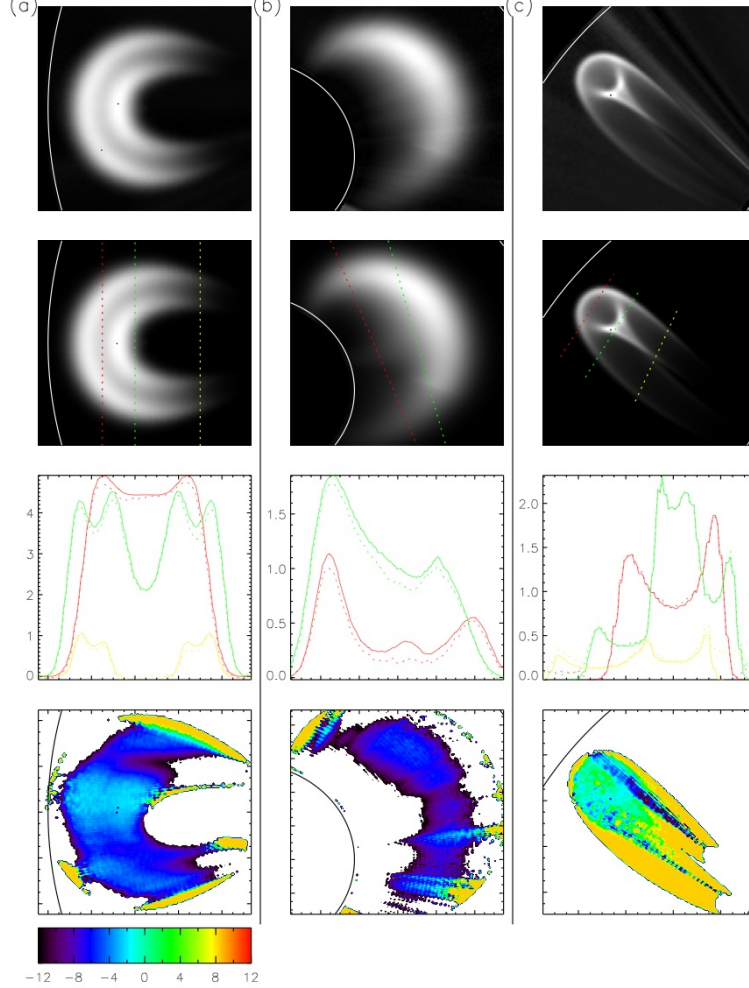


FIG. 9.— Same as figure 8, but for the C3-type FOV.

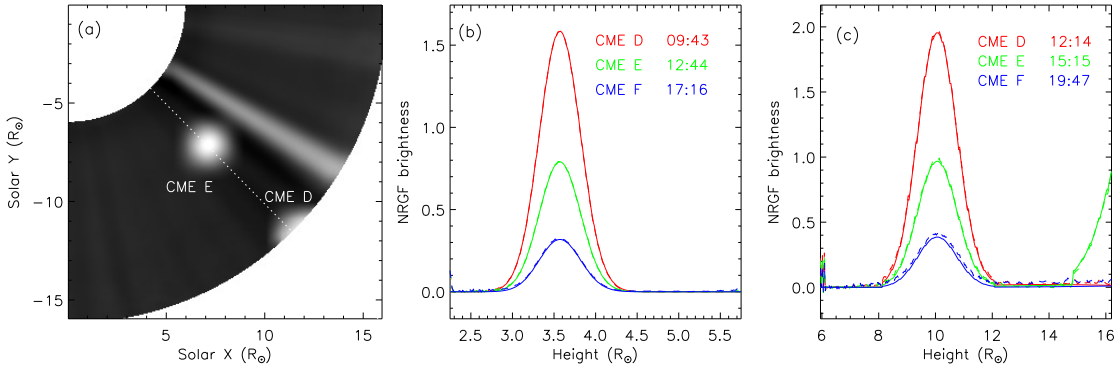


FIG. 10.— (a) The South-west corona for the C3-type FOV and time 15:15 on 2005/01/18, showing a radial slice along position angle 270° . Two CMEs labelled D and E are propagating along this position angle. CME F has not yet entered the FOV. (b) NRGF brightness profiles along the radial slice at position angle 270° for the C2-type FOV at three different times, indicated in the legend. The model is the solid line, and the separated CME component the dashed line. The match is so well that it is difficult to distinguish between the two lines. The synthetic data is set up in such a way that the three CMEs appear at the same height during these three times. (c) As (b), but for the C3-type FOV.

in revealing the structure of this faint CME suggests its potential effectiveness as a tool for CME study, as will be demonstrated fully in Paper II.

4.3. Application to STEREO SECCHI data

The application of the technique to the COR 2/SECCHI coronagraphs aboard the STEREO spacecraft is successful, but the result lacks the cleanliness of the LASCO separated images. This is due to the larger noise level in the COR 2 instruments when compared to the LASCO coronagraphs at a similar height. However, combining separated dynamic component images for the COR 2 and LASCO C3 instrument leads to a powerful analysis of CME structure. A simple example is demonstrated in figure 13 for a CME viewed during 2011/01/13. During this time, the ahead and behind STEREO spacecraft were separated by almost $\pm 90^\circ$ in Carrington longitude from Earth. What is seen as a bright loop-shaped CME using LASCO is seen as a broad, diffuse halo CME in the north corona by the COR 2 A and B coronagraphs. Since the background quiescent structure (i.e. streamers) is absent from the images, the way is paved for a straightforward 3D structural analysis given some realistic assumptions about the CME structure such as smoothness, continuation and curvature (see Frazin et al. (2009), for example). This approach will be addressed in a future work.

5. DISCUSSION

The multiscale detection algorithms presented in Paper II work best on the normalized brightness images (that is, images which are NRGF-processed to remove the radial gradient). It is not necessary for the purpose of CME detection and tracking to preserve the information on calibrated brightness which the original observation can provide. It is important to realize, however, that once the separation process is applied, the CME or background quiescent component can be converted back to absolute brightness units. As the NRGF is applied using equation 6, the average and standard deviation of brightness as functions of height are recorded. After the separation process, the quiescent component in NRGF brightness units B_{norm} can be converted back to absolute brightness B_{abs} by

$$B_{abs}(r, \phi) = B_{norm}(r, \phi)\sigma(r)_{<\phi>} + I(r)_{<\phi>}, \quad (10)$$

which is simply the reverse of equation 6. This component is suitable for density analysis of the large-scale coronal structure using inversion or tomography, with greatly reduced unwanted contamination by CMEs. Large and bright CMEs can seriously disrupt tomographical reconstructions, particularly during solar maximum. Observational studies of the large-scale coronal structure throughout the solar cycle are made possible by removing CMEs from the coronagraph data (Morgan 2011b,a; Morgan & Habbal 2010b).

The CME component is most simply converted to absolute brightness by

$$C_{abs}(r, \phi) = C_{norm}(r, \phi)\sigma(r)_{<\phi>}, \quad (11)$$

where C_{abs} is the absolute brightness and C_{norm} is the NRGF brightness of the separated CME component. This simple equation is possible since the CMEs have not contributed to the estimate of $I(r)_{<\phi>}$. This component

is appropriate for density analysis of the CME in isolation of the background streamer structure, whilst the NRGF brightness CME component is most appropriate for structural and detection analysis. The validity of inverting the NRGF process to reclaim absolute brightness is illustrated by figure 14, where the absolute brightness of the separated CME component of two of the model CMEs (gained by NRGF, the separation technique, then applying equation 11) is compared directly with the target absolute brightness CMEs calculated directly from the model. The agreement is excellent.

There are three main developments which will improve the CME separation process in future work:

- Non-radial quiescent structure can be wrongly included as part of the CME separated image. The technique as presented in this article, therefore, is not suitable for instruments which observe the lower corona. However, if the quiescent coronal structure has a persistent non-radial shape, which changes only slowly, it is possible to envisage a scheme which allows deconvolution along appropriate non-radial directions. The authors are considering such an approach for the high-quality observations of the Atmospheric Imaging Assembly (AIA) instrument aboard the Solar Dynamics Observatory (SDO) (Lemen et al. 2011).
- CME-streamer interaction makes it difficult to distinguish between CME activity and changes in streamer brightness and position. The model used to test the method in this article had CMEs propagating in the same space as quiescent coronal structures, but without interaction. CMEs affect streamer density and distribution, and such changes are rapid. The CME separation process, similarly to time-differencing or other CME analysis techniques (including human recognition), cannot distinguish such effects. Since the quiescent structure can change rapidly, such events will be included in the dynamic component images, although they are not part of a propagating CME. Higher level criteria, such as consideration of outward propagation, may help in discarding such events in the case of automated CME detection and tracking (see Paper II).
- As shown for the model tests, small systematic errors occur according to the apparent propagation speed and type of CME. These are not errors which will hinder the automated detection and analysis routines presented in Paper II, but will influence any density diagnostic. Despite this, to achieve effective density diagnostics, separation must be used. The errors involved are far less than those introduced by using simple time differencing to reveal CME signal, for example. In fact, the errors inherent in the radiometric calibration of coronagraphs, and other uncertainties related to F-corona and stray light subtraction (see Morgan & Habbal (2007c) for example) will in the case of most bright CMEs outweigh any systematic errors introduced by the separation method.

6. CONCLUSIONS

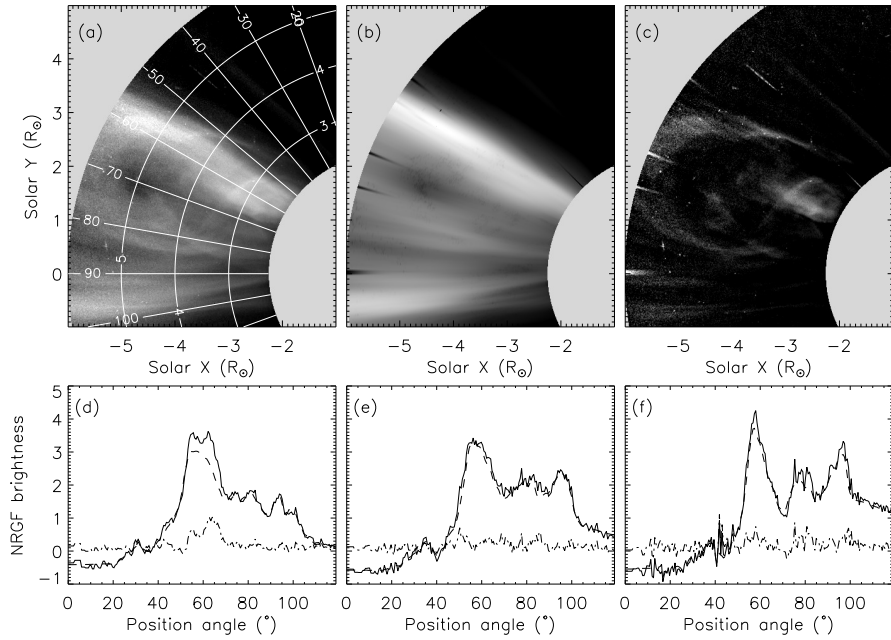


FIG. 11.— (a) NRGF-processed LASCO C2 image of the north-east corona at 2010/03/12 05:06. A faint CME is propagating and interacting with a streamer complex centered on position angle 70° . Position angles are plotted on the image, as are three heights of 3, 4 and $5R_\odot$. (b) The quiescent component following the separation method. (c) The CME component following separation. (d) NRGF brightness plotted as a function of position angle at a constant height of $3R_\odot$. The three lines are for the original NRGF image (solid), the separated quiescent component (dash) and CME component (dash-dot). (e), (f) Same as (d), but for heights of 4 and $5R_\odot$ respectively.

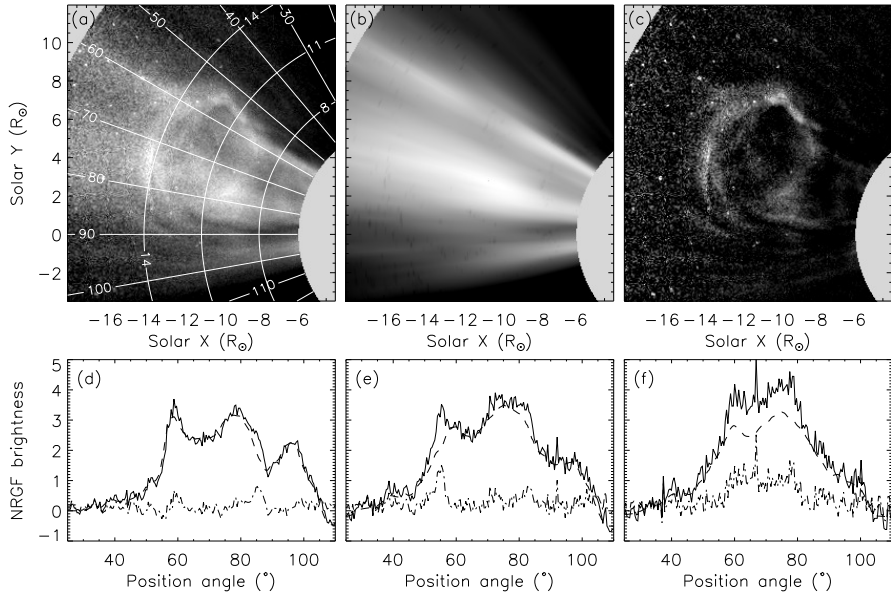


FIG. 12.— Same as figure 11, but for a LASCO C3 observation at 2010/03/12 11:42. The same CME as shown in figure 11 has propagated to the C3 FOV. The three heights shown are 8, 11 and $14R_\odot$.

By means of synthetic coronagraph observations gained from a model corona through which flux-rope and blob-type CMEs are propagated, a deconvolution-based technique is shown to be an effective method to separate the images into quiescent and dynamic components. The dynamic component contains the CME signal which is shown to have excellent agreement (to within a few percent) with direct observations of the CME model made in the absence of the quiescent corona. The technique is

effective with halo, highly-structured CMEs, and small blob-type CMEs, even with density as low as 10% that of streamers at a similar height.

The method is applied to C2 and C3 observations of a very faint CME which is propagating in the same region as a complex arrangement of bright streamers. The method works well despite this challenging data, and the faint CME structure is isolated. We also show the method to be effective with the noisier data of the COR

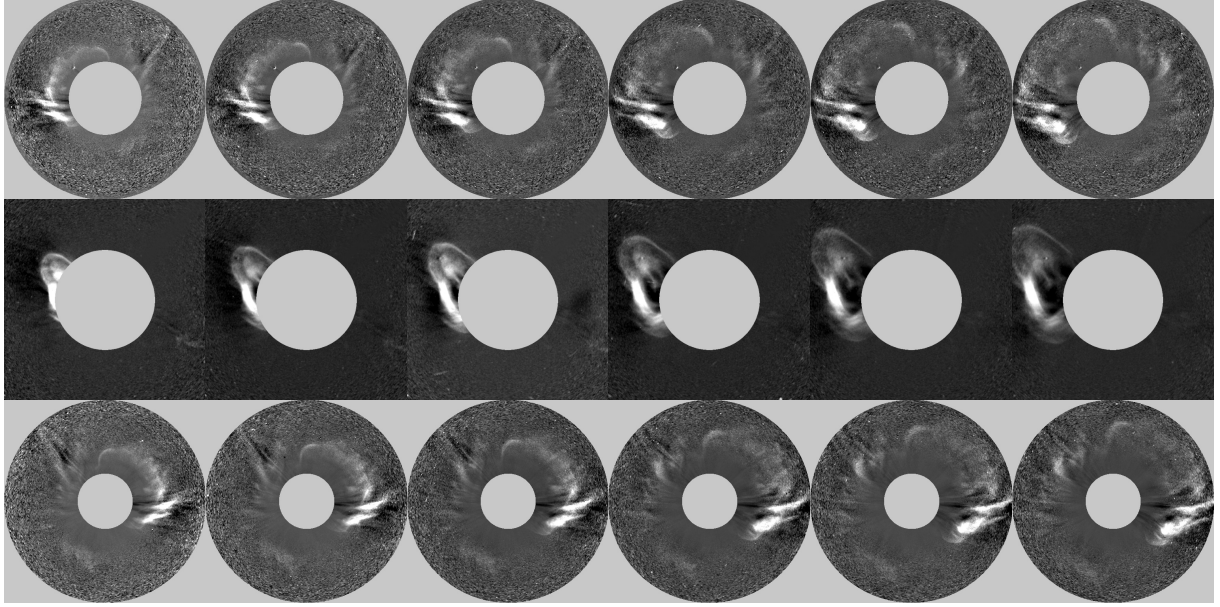


FIG. 13.— Separated dynamic component images of a CME observed during 2011/01/13 by COR2 B (upper row), LASCO C3 (middle row) and COR2 A (bottom row). Times of observation for COR2 A and B are 11:24, 11:39, 11:54, 12:24, 12:39 and 12:54. The LASCO C3 observations are made within a few minutes of the COR observation. All the images are scaled to the same size, with the outer field of view set at $12R_{\odot}$.

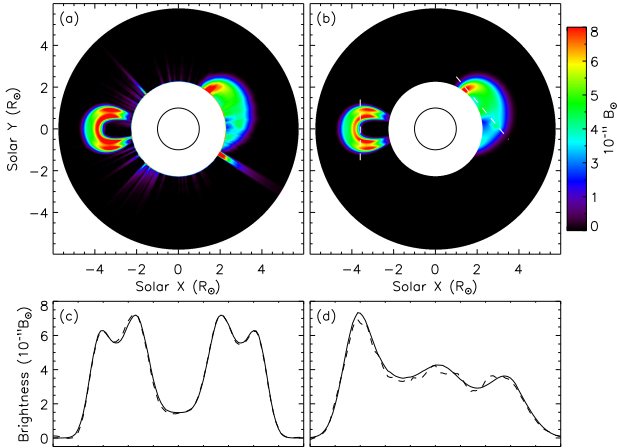


FIG. 14.— (a) Separated CME component for the synthetic observation of 2005/01/19 01:10 (C2 FOV), converted to absolute units using equation 11. The color is scaled as shown in the color bar on the right. (b) Direct synthetic observations of the model CMEs in the absence of background quiescent corona and noise. Two cuts are shown with white dashed lines - one across CME A in the east, and another across CME C in the north west. (c) Brightness across CME A for the directly observed brightness (solid line) and the separated component (dashed line). (d) As (c) but for the cut across CME C.

2 A and B coronagraphs which are part of the SECCHI package of the STEREO mission. This enables straightforward analysis of CME 3D structure using the three

points of view using the dynamic images without the distraction of background streamer structure.

The separation method involves normalizing the data to remove the sharp radial gradient of brightness prior to separation. After separation, the CME and quiescent components can be easily transformed back into absolute brightness units for further density analysis if this is desired. Using the synthetic model images we show this reverse transformation to be very accurate, and faithful to the original model brightness to within a few percent.

The separation of quiescent corona and dynamic events in coronagraph images described in this paper is a necessary prerequisite for higher level CME detection, tracking and classification procedures to be described in Paper II. In the near future, the whole LASCO C2 and C3, and the SECCHI COR 2 dataset will be processed and both quiescent and dynamic component images will be made available to the community.

This work is supported by SHINE grant 0962716 and NASA grant NXXXXXXX to the Institute for Astronomy. The SOHO/LASCO data used here are produced by a consortium of the Naval Research Laboratory (USA), Max-Planck-Institut fuer Aeronomie (Germany), Laboratoire d'Astronomie (France), and the University of Birmingham (UK). SOHO is a project of international cooperation between ESA and NASA.

REFERENCES

- Bewsher, D., Harrison, R. A., & Brown, D. S. 2008, A&A, 478, 897
 Brueckner, G. E., et al. 1995, Sol. Phys., 162, 357
 Byrne, J. P., Gallagher, P. T., McAteer, R. T. J., & Young, C. A. 2009, A&A, 495, 325
 Byrne, J. P., Morgan, H., & Habbal, S. R. 2011, ApJ, 000, 000
 Doyle, J. G., Teriaca, L., & Banerjee, D. 1999, A&A, 349, 956
 Druckmüllerová, H., Morgan, H., & Habbal, S. R. 2011, ApJ, 737, 88
 Eddy, J. A. 1974, A&A, 34, 235
 Frazin, R. A., Jacob, M., Manchester, W. B., Morgan, H., & Wakin, M. B. 2009, ApJ, 695, 636

- Gibson, S. E., Foster, D. J., Guhathakurta, M., Holzer, T., & St. Cyr, O. C. 2003, *Journal of Geophysical Research (Space Physics)*, 108, 7
- Gopalswamy, N., Yashiro, S., Kaiser, M. L., Howard, R. A., & Bougeret, J.-L. 2001, *J. Geophys. Res.*, 106, 29219
- Gosling, J. T., Hildner, E., MacQueen, R. M., Munro, R. H., Poland, A. I., & Ross, C. L. 1974, *J. Geophys. Res.*, 79, 4581
- Guhathakurta, M., Holzer, T. E., & MacQueen, R. M. 1996, *ApJ*, 458, 817
- Habbal, S. R., Morgan, H., Johnson, J., Arndt, M. B., Daw, A., Jaeggli, S., Kuhn, J., & Mickey, D. 2007, *ApJ*, 663, 598
- Habbal, S. R., et al. 2011, *ApJ*, 734, 120
- He, J., Marsch, E., Tu, C., & Tian, H. 2009, *ApJ*, 705, L217
- Howard, R. A., Moses, J. D., Socker, D. G., Dere, K. P., & Cook, J. W. 2002, *Advances in Space Research*, 29, 2017
- Kienreich, I. W., Temmer, M., & Veronig, A. M. 2009, *ApJ*, 703, L118
- Lemen, J. R., et al. 2011, *Sol. Phys.*, 172
- Lugaz, N., Vourlidas, A., Roussev, I. I., & Morgan, H. 2009, *Sol. Phys.*, 256, 269
- Morgan, H. 2011a, *ApJ*, 738, 190
- . 2011b, *ApJ*, 738, 189
- Morgan, H., & Habbal, S. 2010a, *ApJ*, 711, 631
- Morgan, H., & Habbal, S. R. 2007a, *A&A*, 464, 357
- . 2007b, *A&A*, 465, L47
- . 2007c, *A&A*, 471, L47
- . 2010b, *ApJ*, 710, 1
- Morgan, H., Habbal, S. R., & Lugaz, N. 2009, *ApJ*, 690, 1119
- Morgan, H., Habbal, S. R., & Woo, R. 2006, *Sol. Phys.*, 236, 263
- Olmedo, O., Zhang, J., Wechsler, H., Poland, A., & Borne, K. 2008, *Sol. Phys.*, 248, 485
- Quémérais, E., & Lamy, P. 2002, *A&A*, 393, 295
- Robbrecht, E., & Berghmans, D. 2004, *A&A*, 425, 1097
- Thernisien, A. F. R., Howard, R. A., & Vourlidas, A. 2006, *ApJ*, 652, 763
- van de Hulst, H. C. 1950, *Bull. Astron. Inst. Netherlands*, 11, 135
- Wang, Y., et al. 2010, *ApJ*, 717, 973
- Yashiro, S., Gopalswamy, N., Michalek, G., St. Cyr, O. C., Plunkett, S. P., Rich, N. B., & Howard, R. A. 2004, *Journal of Geophysical Research (Space Physics)*, 109, 7105